

High-precision star formation efficiency measurements in nearby clouds

Zipeng Hu,¹ Mark R. Krumholz,^{1,2} Riwaj Pokhrel³ and Robert A. Gutermuth⁴

¹Research School of Astronomy and Astrophysics, Australian National University, Canberra, ACT 2611, Australia

²ARC Centre of Excellence for Astronomy in Three Dimensions (ASTRO-3D), Canberra, ACT 2611, Australia

³Ritter Astrophysical Research Center, Department of Physics and Astronomy, University of Toledo, Toledo, OH 43606, USA

⁴Department of Astronomy, University of Massachusetts, 710 North Pleasant Street, Amherst, MA 01003, USA

Accepted XXX. Received YYY; in original form ZZZ

ABSTRACT

On average molecular clouds convert only a small fraction ϵ_{ff} of their mass into stars per free-fall time, but differing star formation theories make contrasting claims for how this low mean efficiency is achieved. To test these theories, we need precise measurements of both the mean value and the scatter of ϵ_{ff} , but high-precision measurements have been difficult because they require determining cloud volume densities, from which we can calculate free-fall times. Until recently, most density estimates assume clouds as uniform spheres, while their real structures are often filamentary and highly non-uniform, yielding systematic errors in ϵ_{ff} estimates and smearing real cloud-to-cloud variations. We recently developed a theoretical model to reduce this error by using column density distributions in clouds to produce more accurate volume density estimates. In this letter, we apply this model to recent observations of 12 nearby molecular clouds. Compared to earlier analyses, our method reduces the typical dispersion of ϵ_{ff} within individual clouds from 0.35 dex to 0.31 dex, and decreases the median value of ϵ_{ff} over all clouds from ≈ 0.02 to ≈ 0.01 . However, we find no significant change in the ≈ 0.2 dex cloud-to-cloud dispersion of ϵ_{ff} , suggesting the measured dispersions reflect real structural differences between clouds.

Key words: stars: formation – ISM: structure.

1 INTRODUCTION

Star formation is inefficient. A star forming region with little resistance to self-gravity will convert its gaseous mass to stars within a single free-fall time $t_{\text{ff}} = \sqrt{3\pi/32G\rho}$, where ρ is the volume density; the ratio of the actual star formation rate to this maximum is called the efficiency per free-fall time ϵ_{ff} (Krumholz & McKee 2005). Zuckerman & Evans (1974) were the first point out that the observed star formation rate of the Milky Way as a whole implies that, averaged over all molecular clouds, $\epsilon_{\text{ff}} \sim 0.01$. Krumholz & Tan (2007) extended this conclusion to the denser parts of molecular clouds traced by HCN, and more recent work has obtained similar means both for clouds traced by dust (e.g., Heyer et al. 2016) and for ~ 100 pc-scale patches in nearby galactic discs (e.g., Utomo et al. 2018). The study-to-study dispersion in ϵ_{ff} is ≈ 0.3 dex, while the dispersion within any single study is about 0.3 – 0.5 dex (Krumholz et al. 2019).

Theoretical efforts to explain the origin of observed low ϵ_{ff} values can be categorized into two main types. Some theories focus on galactic scale physical processes (e.g. Kim et al. 2011; Ostriker & Shetty 2011; Faucher-Giguère et al. 2013), while others are developed from internal star formation regulation processes within individual molecular clouds (e.g. Elmegreen & Parravano 1994; Krumholz et al. 2011a; Federrath & Klessen 2012). Despite predicting similarly-low mean ϵ_{ff} values, the two types of models yield significantly different estimates for the *dispersion* of ϵ_{ff} – models regulated on the cloud

scale generally predict much smaller dispersions than those regulated on the galactic scale (Lee et al. 2016; Krumholz & McKee 2020). Therefore, it is important to measure cloud-scale ϵ_{ff} values with enough fidelity to extract both its mean value and dispersion. The most accurate measurements to date are those of Pokhrel et al. (2021), who determine a median value $\log \epsilon_{\text{ff}} = -1.59$ with a dispersion of 0.18 dex in a sample of 12 nearby molecular clouds.

However, most previous ϵ_{ff} measurements, including those of Pokhrel et al. (2021), incur a substantial error when calculating the volume density, which is required for the free-fall time. The fundamental challenge is that the volume density is a three-dimensional quantity, which is not directly accessible in a two-dimensional observation. The most common practice in literature is to estimate the density by assuming that the area of interest is the projection of a uniform sphere, whose radius is equal to the mean radius of the projected shape. For a cloud with a total projected area A and a total mass M , this approximation gives a density estimate $\rho_{\text{sph}} = 3M/4\sqrt{A^3/\pi}$. This method has been used by a number of authors in the Milky Way (e.g., Krumholz et al. 2011b; Lada et al. 2013; Evans et al. 2014; Pokhrel et al. 2021) and in the Large Magellanic Cloud (Ochsendorf et al. 2017). While simple, this procedure likely introduces significant systematic errors, coming from two primary sources. One is that in the past decades, it has become clear that the interstellar medium is characterised mainly by filamentary structures (e.g. Schneider & Elmegreen 1979; Dobashi et al. 2005; Arzoumanian et al. 2011; André et al. 2014; Kainulainen et al. 2016), which results in elongated contours identified from column density maps. The mean density of

* zphu.charles@gmail.com (ZPH)

such structure is likely to be different from that calculated with spherical assumption. Second, the free-fall time computed from the mean volume density is not identical to the mean free-fall time, because the relationship between the two, $t_{\text{ff}} \propto \rho^{-1/2}$, is non-linear. The quantity of interest for ϵ_{ff} is the mass-weighted mean of $1/t_{\text{ff}}$, and this mean can differ substantially from the overall mean density (e.g. [Hennebelle & Chabrier 2011](#); [Federrath & Klessen 2012](#); [Federrath 2013](#); [Salim et al. 2015](#)).

[Hu et al. \(2021\)](#) recently proposed an alternative approach to estimate the free-fall time weighted mean density ρ_{eff} , which immediately yields the correct free-fall time for the purposes of estimating ϵ_{ff} . [Hu et al.](#) analyse star formation simulations from [Cunningham et al. \(2018\)](#), and show that one can estimate ρ_{eff} with higher accuracy than is obtained from the simple spherical assumption by making use of the full two-dimensional (2D) column density distribution, rather than simply its mean. Applied to simulations, their method corrects a ≈ 0.13 dex overestimate and removes a ~ 0.25 dex scatter in ϵ_{ff} caused by spherical assumption. In this paper, we apply this model to the observations of [Pokhrel et al. \(2020, 2021\)](#) in order to derive higher-accuracy ϵ_{ff} measurements than have previously been possible. We summarise the observations in [Section 2](#), describe how we apply the [Hu et al.](#) method to them in [Section 3](#), present the results of the analysis in [Section 4](#), and draw conclusions in [Section 5](#).

2 OBSERVATIONS

Our data reduction and analysis method is described in [Pokhrel et al. \(2020\)](#), and full details are provided there. Here we simply summarise for convenience. This study analyses 12 nearby star forming regions: Ophiuchus, Perseus, Orion-A, Orion-B, Aquila-North, Aquila-South, NGC 2264, S140, AFGL 490, Cep OB3, Mon R2, and Cygnus-X. For each region we have a matched protostellar catalogue and cloud column density map. The latter are derived from *Herschel*/PACS and *Herschel*/SPIRE imaging at 160, 250, 350, and 500 μm , convolved to a common resolution ([André et al. 2010](#)). To obtain the column density in each pixel, we fit the spectral energy distribution with a dust emission model where the only two free parameters are the temperature and the column density. The best-fitting column density can be equivalently expressed in column of H_2 molecules, $N(\text{H}_2)$, or column of gas mass σ_{gas} , which are related by $\Sigma_{\text{gas}} = 2m_{\text{H}}/XN(\text{H}_2)$, where $m_{\text{H}} = 1.67 \times 10^{-24}$ g is the hydrogen atom mass and $X = 0.71$ is the hydrogen mass fraction of the local interstellar medium ([Nieva & Przybilla 2012](#)). On the obtained column density map, we first mask pixels with the best-fitting dust temperature exceeds the Rayleigh–Jeans (R-J) limit, since such pixels are in the R-J limit for all the *Herschel* bands, and thus the fits are highly uncertain. The exact temperature limits are provided in Table 2 of [Pokhrel et al. \(2020\)](#). Second, we mask pixels with derived column densities $N(\text{H}_2) > 10^{23} \text{ cm}^{-2}$, because for these dust optical depth effects can be significant and thus fitted $N(\text{H}_2)$ values may only represent lower limits. The effect of both masks is negligible in our results, since the number of masked pixels is very small, and, for many clouds, zero.

The SESNA catalog (R. Gutermuth et al., in preparation) we use for protostars is a combination of *Spitzer* and Two Micron All-Sky Survey observations (2MASS; [Skrutskie et al. 2006](#)), spanning about 90 deg^2 . For the farthest target Cygnus-X, the deeper UKIDSS ([Lawrence et al. 2007](#)) near-IR Galactic Place Survey ([Lucas et al. 2008](#)) is used. We mask parts of column density maps outside SESNA coverage. After subtracting field stars, sources with excess IR emission are classified into different types of young stellar object (YSO) and contaminant by using flux selections and a series of reddening-

safe color ([Gutermuth et al. 2009](#)). Hence the total number of protostars N_{PS} in any enclosed contour on the column density map can be calculated after contamination correction, whose detailed procedure is provided in [Pokhrel et al. \(2020\)](#).

3 METHODS

The first step of our analysis is to generate column density contours across the full range of $N(\text{H}_2)$ covered by the observations. For each of the 12 regions, we start by finding the lowest $N(\text{H}_2)$ value such that all pixels with column density above it are inside the SESNA coverage; equivalently, we set the minimum value of $N(\text{H}_2)$ to be the lowest possible choice such that the contour sits entirely within the SENSEA footprint. We define M_0 as the total gas mass enclosed by this contour. We then draw 100 $N(\text{H}_2)$ contours at higher $N(\text{H}_2)$, with the levels chosen such that the total mass above each level is equally spaced from M_0 to $M_0/100$ with a step of $M_0/100$. We show an example of Ophiuchus cloud column density map with $N(\text{H}_2)$ contours, protostar positions, and SESNA coverage area in [Figure 1](#).

For every contour, we measure four values: total gas mass M_{gas} , total area A , completeness-corrected total protostar number N_{PS} and the Gini coefficient g of the surface density of all pixels within the contour (see [Hu et al. 2021](#) for details). From these parameters we derive 4 additional quantities: mean gas surface density $\Sigma_{\text{gas}} = M_{\text{gas}}/A$, star formation surface density Σ_{SFR} , the free-fall time derived from the spherical assumption $t_{\text{ff,sph}}$ (see [Section 1](#)), and the corresponding star formation efficiency per free fall time $\epsilon_{\text{ff,sph}}$. To calculate Σ_{SFR} , we assume the mean mass of protostars in SESNA to be $M_{\text{PS}} \approx 0.5M_{\odot}$ ([Evans et al. 2009](#)), and the mean duration of protostellar phase included in SESNA observations to be $t_{\text{PS}} \approx 0.5 \text{ Myr}$ ([Dunham et al. 2014, 2015](#)). Thus, $\Sigma_{\text{SFR}} = N_{\text{PS}}M_{\text{PS}}/At_{\text{PS}}$, and $\epsilon_{\text{ff,sph}} = \Sigma_{\text{SFR}}/(\Sigma_{\text{gas}}/t_{\text{ff,sph}})$.

Our next step is to apply the correction obtained by [Hu et al. \(2021\)](#), who find a relation between free-fall time weighted mean density ρ_g and ρ_{sph} :

$$\rho_g = 10^{kg-b} \rho_{\text{sph}}, \quad (1)$$

with $k = 4.6$ and $b = 0.93$. Replacing ρ_{sph} with ρ_g gives us the corrected values of free-fall time $t_{\text{ff,g}}$ and star formation efficiency per free-fall time $\epsilon_{\text{ff,g}}$. In order to accomplish our goal of obtaining high-accuracy estimates of ϵ_{ff} , it is important to understand the uncertainties in this relation. Although the values of k and b are fitted from exact simulation data without error bars, we can obtain estimate of the errors on these quantities from bootstrapping. We randomly choose half of the simulation sample to fit [equation 1](#), repeating this process 10^4 times. We take our uncertainties to be the 16th and 84th percentiles of the fitted k and b values, which give $k = 4.6 \pm 0.1$ and $b = 0.93 \pm 0.03$. We show below that these uncertainties are small enough that they contribute negligibly to the overall error budget.

We next remove from our sample contours small enough that beam-smearing precludes an accurate estimate of g . To do so, for each contour we compute the ratio of the mean contour radius $r = \sqrt{A/\pi}$ to the resolution R on the *Herschel* maps (expressed as the effective beam FWHM, taken from Table 1 of [Pokhrel et al. 2020](#)). To check when beam smearing becomes significant, we artificially blur our data: for each cloud we construct 8 column density maps smeared by Gaussian beams with sizes uniformly spaced between R and $20R$, and place contours on these smeared maps exactly as we do for the original maps. We plot the distribution of g values for all contours with $\Sigma_{\text{SFR}} > 0$ in [Figure 2](#). The figure clearly shows the expected effect: contours with small r/R have systematically

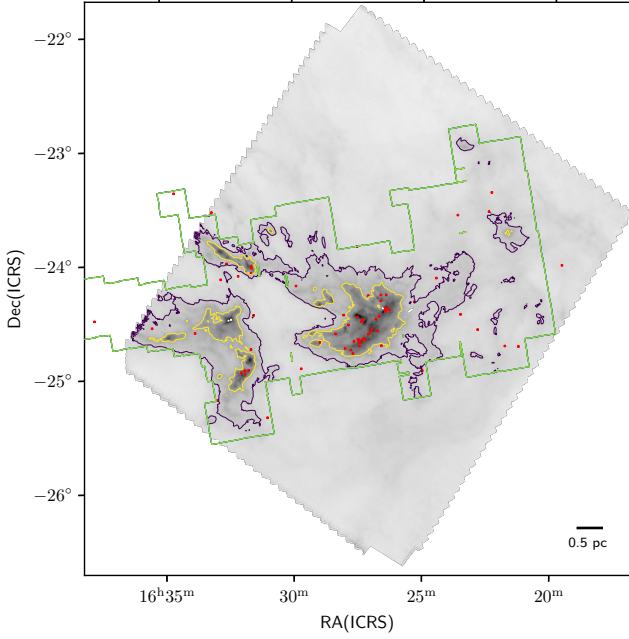


Figure 1. A column density map of the Ophiuchus Cloud derived from *Herschel* observations. The green contour is the Spitzer coverage area, and we illustrate the largest contour that fits within this footprint in purple; the yellow contour is set at a level that encloses half as much mass as the purple one. The red dots are the positions of YSOs.

smaller values of g than larger ones. To quantify this, we fit the distribution of $(\log(r/R), g)$ values with a piece-wise linear function $g = k [\log(r/R) - x_0] + y_0$ for $\log(r/R) < x_0$, and $g = y_0$ otherwise, where k , x_0 , and y_0 are free parameters. The green line shows the best fit, $k = 0.47$, $x_0 = 0.95$, and $y_0 = -0.65$, which illustrates the effect in which we are interested: the distribution of g values becomes independent of resolution when $\log(r/R) \geq 0.95$, and drops below this threshold. We therefore remove from our analysis of the original, unsmeared maps any contour with $\log(r/R) < 0.95$. We also include only contours that contain at least one protostar, since we obviously cannot compute ϵ_{ff} values for those that contain none. After this down-select we obtain 3410 contours that form the data set for further analysis.

4 RESULTS

With the properties determined from the unsmeared contours on different surface density levels, we first investigate how the triplet $(g, \epsilon_{\text{ff,sph}}, \epsilon_{\text{ff,g}})$ changes with Σ_{gas} . In Figure 3 we show the scatter plot of g versus $\log(\Sigma_{\text{gas}})$, which presents a clear trend of g decreasing with Σ_{gas} . It is important to note that this is *not* a resolution effect, since we have removed contours small enough that lack of resolution leads to them being blurred; instead, it is a real physical trend. The median value of g is $g_{\text{median}} = 0.24$, which is above 0.2, the value for a uniform-density sphere (Hu et al. 2021). This indicates that the free-fall time of most contours will be overestimated by the spherical assumption. For a typical Gini coefficient $g = 0.24$, our estimated uncertainties on k and b in equation 1 translate to an increase in the dispersion of ϵ_{ff} by 0.01 dex, which is negligible. For this reason, we will simply treat k and b as constants fixed to their central values for the remainder of this analysis.

To study the difference between estimates of ϵ_{ff} derived using

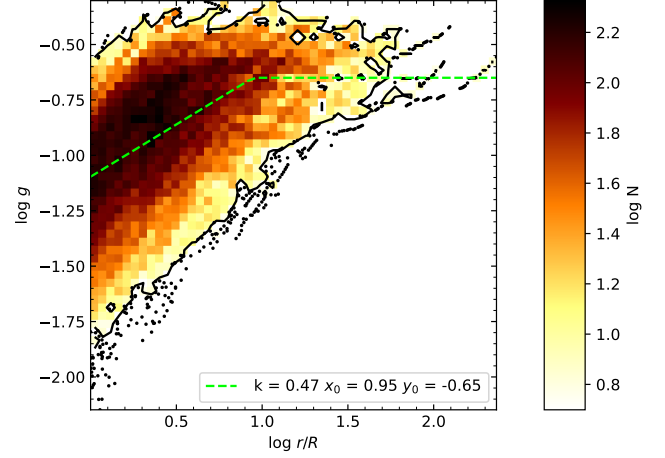


Figure 2. 2D distribution plot of g versus $\log(r/R)$. The values are determined from the smeared contours, and the color shows the number of contours in each bin (one black dot represents one single contour). The green dash line shows a piecewise linear fit to this distribution.

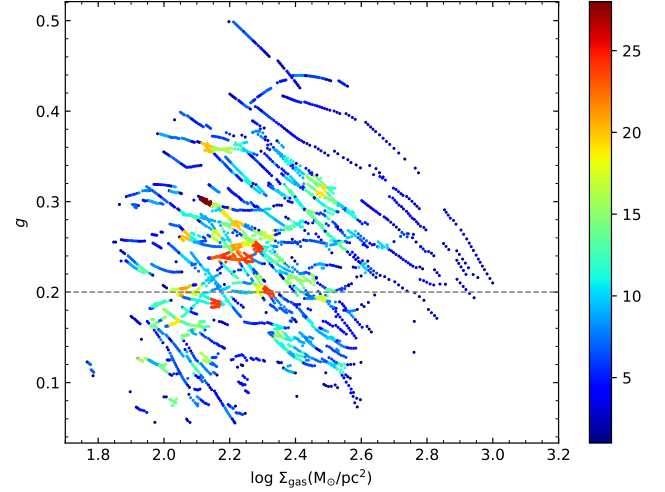


Figure 3. 2D scatter plot of g versus $\log(\Sigma_{\text{gas}})$. The values are determined from the unsmeared contours, and the color shows the number of contours in the scatter circle. The grey dash line shows the $g = 0.2$ reference line for the projection of a uniform sphere.

the spherical assumption and our improved method, we define two quantities: the mean star formation efficiency for an individual cloud $\langle \epsilon_{\text{ff}} \rangle$, and the mean dispersion in star formation efficiency σ . We compute these as follows: for each cloud, we sort the contours by Σ_{gas} and place them in 10 bins of equal size, or fewer if that leaves a cloud with < 20 contours per bin. (Recall that Σ_{gas} is the mean surface density inside a given contour, not the contour level itself, so two contours at the same level still generally have different Σ_{gas} .) Within each bin, we denote the 16th, 50th, and 84th percentiles of ϵ_{ff} (for both $\epsilon_{\text{ff,sph}}$ and $\epsilon_{\text{ff,g}}$) as $\epsilon_{\text{ff},16}$, $\epsilon_{\text{ff},50}$, and $\epsilon_{\text{ff},84}$. We plot these quantities as a function of Σ_{gas} in Figure 4. We then define the mean star formation efficiency for one cloud $\langle \epsilon_{\text{ff}} \rangle$ as

$$\langle \epsilon_{\text{ff}} \rangle = \frac{\int_{\log \Sigma_{\text{gas},\text{min}}}^{\log \Sigma_{\text{gas},\text{max}}} \epsilon_{\text{ff},50}(\Sigma_{\text{gas}}) d(\log \Sigma_{\text{gas}})}{\log \Sigma_{\text{gas},\text{max}} - \log \Sigma_{\text{gas},\text{min}}}, \quad (2)$$

where $\Sigma_{\text{gas},\text{min}}$ and $\Sigma_{\text{gas},\text{max}}$ are the minimum and maximum contour

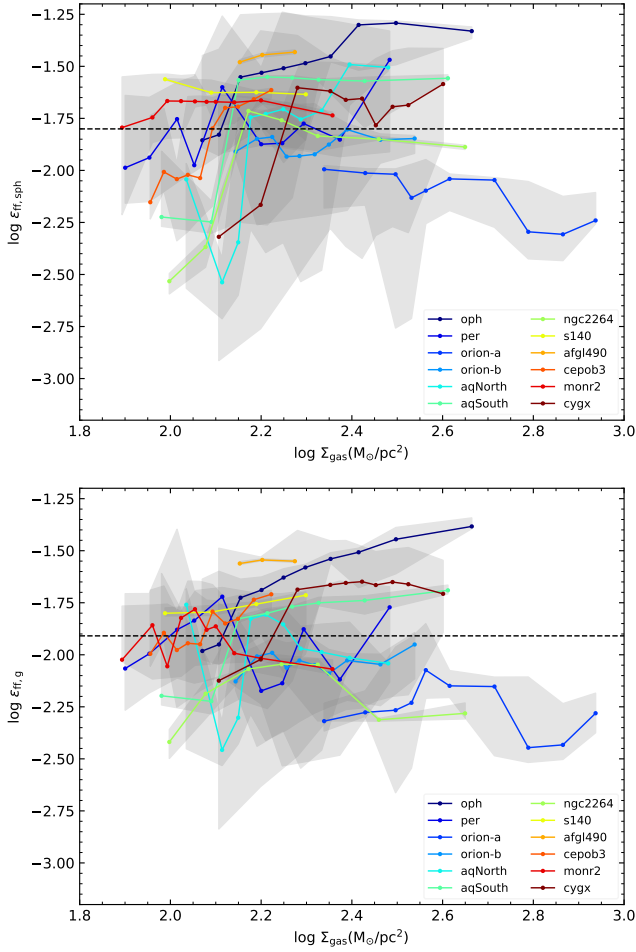


Figure 4. Distributions of $\log \epsilon_{\text{ff},\text{sph}}$ (top) and $\log \epsilon_{\text{ff},\text{g}}$ (bottom) as a function of $\log \Sigma_{\text{gas}}$. For each cloud, the coloured line and grey band show the 50th percentile and 16th–84th percentile range of ϵ_{ff} in a bin of $\log \Sigma_{\text{gas}}$. The black dashed lines show the median values $\langle \epsilon_{\text{ff},\text{sph}} \rangle$ and $\langle \epsilon_{\text{ff},\text{g}} \rangle$ over all clouds.

surface density available for a given cloud; in terms of Figure 4, $\langle \epsilon_{\text{ff}} \rangle$ is simply the mean value of the coloured line for each cloud. We evaluate this integral by approximating it as a finite sum over our groups. Similarly, we define the mean star formation efficiency dispersion σ as

$$\sigma = \frac{\int_{\log \Sigma_{\text{gas},\text{min}}}^{\log \Sigma_{\text{gas},\text{max}}} (\log \epsilon_{\text{ff},84}(\Sigma_{\text{gas}}) - \log \epsilon_{\text{ff},16}(\Sigma_{\text{gas}})) d(\log \Sigma_{\text{gas}})}{\log \Sigma_{\text{gas},\text{max}} - \log \Sigma_{\text{gas},\text{min}}}, \quad (3)$$

where we again evaluate numerically as a finite sum over our bins of Σ_{gas} . In terms of Figure 4, σ is simply the mean width of the grey band that surrounds each of the coloured lines.

We report the $\langle \epsilon_{\text{ff}} \rangle$ and σ values we measure using the spherical assumption (denoted by subscript sph) and with equation 1 (subscript g) for all 12 clouds in Table 1. After applying our model, the median value of $\log \langle \epsilon_{\text{ff}} \rangle$ decreases from $\log \langle \epsilon_{\text{ff},\text{sph}} \rangle = -1.80$ to $\log \langle \epsilon_{\text{ff},\text{g}} \rangle = -1.91$. This is consistent with the prediction in Hu et al. (2021) that use of the spherical assumption leads to a ~ 0.13 dex overestimate of ϵ_{ff} . We also measured the difference in dispersion $\Delta\sigma = \sigma_{\text{sph}} - \sigma_{\text{g}}$ derived using the spherical assumption versus using equation 1 for each cloud. We find that 8 of the 12 studied clouds yield positive $\Delta\sigma$, corresponding to a reduction in the dispersion; the median reduction

Cloud	$\log \langle \epsilon_{\text{ff},\text{sph}} \rangle$	$\log \langle \epsilon_{\text{ff},\text{g}} \rangle$	σ_{sph} (dex)	σ_{g} (dex)	$\Delta\sigma$ (dex)	$\log \Sigma_{\text{gas}}$ (M_{\odot}/pc^2)
Ophiuchus	-1.44	-1.57	0.35	0.25	0.10	(2.05, 2.79)
Perseus	-1.80	-1.96	0.56	0.62	-0.06	(1.85, 2.67)
Orion-A	-2.12	-2.27	0.32	0.31	0.01	(2.24, 3.00)
Orion-B	-1.87	-2.03	0.38	0.31	0.07	(2.10, 2.64)
Aquila-N	-1.84	-2.02	0.56	0.44	0.12	(2.02, 2.56)
Aquila-S	-1.71	-1.86	0.30	0.23	0.07	(1.92, 2.78)
NGC 2264	-1.94	-2.19	0.06	0.11	-0.05	(1.97, 2.77)
S140	-1.62	-1.77	0.07	0.07	0.00	(1.95, 2.36)
AFGL 490	-1.45	-1.55	0.02	0.01	0.01	(2.14, 2.32)
Cep OB3	-1.86	-1.86	0.36	0.30	0.06	(1.92, 2.41)
Mon R2	-1.70	-1.97	0.17	0.20	-0.03	(1.77, 2.48)
Cygnus-X	-1.80	-1.77	1.02	0.89	0.13	(1.90, 2.78)
Median	-1.80	-1.91	0.34	0.28	0.03	
Mean	-1.76	-1.90	0.35	0.31	0.03	
STD	0.19	0.21				

Table 1. Estimates of $\langle \epsilon_{\text{ff}} \rangle$ and σ for individual clouds, using both the spherical assumption (values with subscript “sph”) and the Gini model equation 1 (values with subscript “g”); $\Delta\sigma = \sigma_{\text{sph}} - \sigma_{\text{g}}$. The column $\log \Sigma_{\text{gas}}$ reports the (min, max) surface density measured for each cloud. Finally, the last three rows list the median, mean, and standard deviation values (STD) of the corresponding columns.

is $\Delta\sigma_{\text{median}} = 0.03$ dex. This demonstrates that our model does decrease the dispersion, but less than the ~ 0.15 dex found when testing the method on simulated data in Hu et al. (2021). This is likely due to the difference between the simulated data and observations. Hu et al. (2021) calibrate their method based on simulations from Cunningham et al. (2018) that use periodic boundary conditions, so the column density maps used in the calibration are from infinitely large self-similar clouds. The observed clouds, however, are from finite size, so, for example, they can contain large-scale density gradients that are absent in periodic boxes. This suggests that we might obtain an improved version of equation 1 by analyzing a zoom-in galactic simulation.

For all 12 clouds, we determine the standard deviations (STD) of both types of $\langle \epsilon_{\text{ff}} \rangle$ values: $\text{STD}_{\text{sph}} = 0.19$, and $\text{STD}_{\text{g}} = 0.21$. The difference is not significant, but this is perhaps not surprising because even with the spherical assumption the dispersion of ≈ 0.2 is very small, and may well reflect real physical differences between clouds, as we discuss below. Given the relatively small $\Delta\sigma_{\text{median}}$ we obtain, it is also interesting to ask whether we could forgo individualized corrections altogether, and simply adopt the median value $g = 0.24$ for all contours. Doing so would still produce a 0.1 dex median value decrease in ϵ_{ff} , while leaving the dispersion unchanged. However, such an approach would miss an important subtlety: while $g = 0.24$ is the median value for all contours on all scales, the value of g also changes systematically with size scale: on the largest scales of the 12 clouds we study, $g_{\text{median}} = 0.35$. Properly accounting for this is crucial to obtaining the correct changes in ϵ_{ff} versus Σ_{gas} , and thus the correct $\Delta\sigma$ values within individual clouds. For this reason, we prefer to use individual-contour corrections when possible.

5 CONCLUSIONS

We use a new method proposed by Hu et al. (2021) to combine column density maps derived from *Herschel* with young stellar objects from the SESNA catalog to determine the star formation efficiency per free-fall time ϵ_{ff} in 12 nearby clouds. Our method provides a

more realistic estimate of the mean volume densities of clouds seen in projection, substantially reducing the error incurred by assuming that projected clouds are spherical, and allowing higher-precision estimates of ϵ_{ff} than previously possible. We find that the spherical assumption leads to ~ 0.1 dex overestimate of $\log\langle\epsilon_{\text{ff}}\rangle$, and also increases the estimated intra-cloud dispersion in $\log\langle\epsilon_{\text{ff}}\rangle$ by ~ 0.03 dex on average. With our new method, we find that our sample of 12 clouds has a median star formation efficiency per free-fall time $\log\langle\epsilon_{\text{ff}}\rangle = -1.9$, and the median spread in $\log\langle\epsilon_{\text{ff}}\rangle = 0.28$ dex within a single cloud. The inter-cloud dispersion in $\log\langle\epsilon_{\text{ff}}\rangle$ is nearly identical, at 0.21 dex, and this value is, within the uncertainties, unaffected by the use of the [Hu et al. \(2021\)](#) model for the gas density. This strongly suggests that the intra-cloud dispersion we are measuring reflects a real variation in cloud properties, not an observational error.

Our results confirm the existence of a universal $\epsilon_{\text{ff}} \sim 0.01$ value, and, importantly, let us identify a real ≈ 0.2 dex spread from cloud to cloud with 3D cloud geometry considered for the first time. As discussed in [Pokhrel et al. \(2021\)](#), such a small spread is in tension with models where star formation is regulated mainly by galactic-scale processes, but individual molecular clouds undergo rapid collapse. These models predict a much larger dispersion. Conversely, however, our measured spread in ϵ_{ff} can be used to evaluate the spread in parameters that enter models for cloud-scale regulation of star formation, which do predict dispersions comparable in size to the observed one. For example, in the turbulence regulated star formation of [Krumholz & McKee \(2005\)](#), a ~ 0.2 dex spread in ϵ_{ff} could naturally be explained by a $\sigma_{\alpha} \sim 0.3$ dex spread in cloud virial parameters (or a $\sigma_M \sim 0.7$ dex spread in Mach number), while in the similar model of [Hennebelle & Chabrier \(2011\)](#) the required dispersion is $\sigma_{\alpha} \sim 0.8$ dex ($\sigma_M \sim 0.6$ dex), and for the model of [Padoan et al. \(2012\)](#) would require $\sigma_{\alpha} \sim 0.5$ dex. For comparison, [Lee et al. \(2016\)](#) study 195 star forming giant molecular clouds and find a scatter of 0.32 dex in the virial parameter. Thus observed clouds have approximately the level of dispersion in virial parameter required to reproduce the spread we see in ϵ_{ff} . In future work, we can use the same technique of high-precision estimates of ϵ_{ff} deployed here to search not just for the dispersion in ϵ_{ff} , but to look for systematic variations with virial parameter or other cloud properties, thereby opening up a new method for testing theories of star formation.

ACKNOWLEDGEMENTS

MRK acknowledges funding from Australian Research Council awards DP190101258 and FT180100375. RP and RAG acknowledge support from NASA ADAP awards NNX15AF05G, 80NSSC18K1564 and NNX17AF24G. RP acknowledges funding from NASA ADAP award 80NSSC18K1564, and RAG acknowledges funding from NASA ADAP awards NNX11AD14G and NNX13AF08G. We further acknowledge high-performance computing resources provided by the Australian National Computational Infrastructure (grants jh2 and ek9) through the National and ANU Computational Merit Allocation Schemes, and by the Leibniz Rechenzentrum and the Gauss Centre for Supercomputing (grant pr321o).

This research has made use of data from the [Herschel Gould Belt survey \(HGBS\) project](#), a Herschel Key Programme jointly carried out by SPIRE Specialist Astronomy Group 3 (SAG 3), scientists of several institutes in the PACS Consortium (CEA Saclay, INAF-IFSI Rome and INAF-Arcetri, KU Leuven, MPIA Heidelberg), and scientists of the Herschel Science Center (HSC).

DATA AVAILABILITY

The data underlying this article will be shared upon reasonable request to the corresponding author.

REFERENCES

- André P., et al., 2010, [A&A](#), 518, L102
 André P., Di Francesco J., Ward-Thompson D., Inutsuka S.-I., Pudritz R. E., Pineda J., 2014, [Protostars and Planets VI](#)
 Arzoumanian D., et al., 2011, [A&A](#), 529, L6
 Cunningham A. J., Krumholz M. R., McKee C. F., Klein R. I., 2018, [MNRAS](#), 476, 771–792
 Dobashi K., Uehara H., Kandori R., Sakurai T., Kaiden M., Umemoto T., Sato F., 2005, [Publications of the Astronomical Society of Japan](#), 57, S1
 Dunham M. M., et al., 2014, [Protostars and Planets VI](#)
 Dunham M. M., et al., 2015, [ApJS](#), 220, 11
 Elmegreen B. G., Parravano A., 1994, [ApJ](#), 435, L121
 Evans N. J., et al., 2009, [ApJS](#), 181, 321–350
 Evans N. J., Heiderman A., Vutisalchavakul N., 2014, [ApJ](#), 782, 114
 Faucher-Giguère C.-A., Quataert E., Hopkins P. F., 2013, [MNRAS](#), 433, 1970–1990
 Federrath C., 2013, [MNRAS](#), 436, 3167–3172
 Federrath C., Klessen R. S., 2012, [ApJ](#), 761, 156
 Gutermuth R. A., Megeath S. T., Myers P. C., Allen L. E., Pipher J. L., Fazio G. G., 2009, [ApJS](#), 184, 18–83
 Hennebelle P., Chabrier G., 2011, [ApJ](#), 743, L29
 Heyer M., Gutermuth R., Urquhart J. S., Csengeri T., Wienen M., Leurini S., Menten K., Wyrowski F., 2016, [A&A](#), 588, A29
 Hu Z., Krumholz M. R., Federrath C., Pokhrel R., Gutermuth R. A., 2021, [MNRAS](#), 502, 5997–6009
 Kainulainen J., Hacar A., Alves J., Beuther H., Bouy H., Tafalla M., 2016, [A&A](#), 586, A27
 Kim C.-G., Kim W.-T., Ostriker E. C., 2011, [ApJ](#), 743, 25
 Krumholz M. R., McKee C. F., 2005, [ApJ](#), 630, 250–268
 Krumholz M. R., McKee C. F., 2020, [MNRAS](#), 494, 624–641
 Krumholz M. R., Tan J. C., 2007, [ApJ](#), 654, 304–315
 Krumholz M. R., Leroy A. K., McKee C. F., 2011a, [ApJ](#), 731, 25
 Krumholz M. R., Dekel A., McKee C. F., 2011b, [ApJ](#), 745, 69
 Krumholz M. R., McKee C. F., Bland-Hawthorn J., 2019, [Annual Review of Astronomy and Astrophysics](#), 57, 227–303
 Lada C. J., Lombardi M., Roman-Zuniga C., Forbrich J., Alves J. F., 2013, [ApJ](#), 778, 133
 Lawrence A., et al., 2007, [MNRAS](#), 379, 1599–1617
 Lee E. J., Miville-Deschênes M.-A., Murray N. W., 2016, [ApJ](#), 833, 229
 Lucas P. W., et al., 2008, [MNRAS](#), 391, 136–163
 Nieva M.-F., Przybilla N., 2012, [A&A](#), 539, A143
 Ochsendorf B. B., Meixner M., Roman-Duval J., Rahman M., Evans N. J., 2017, [ApJ](#), 841, 109
 Ostriker E. C., Shetty R., 2011, [ApJ](#), 731, 41
 Padoan P., Haugbølle T., Nordlund Å., 2012, [ApJ](#), 759, L27
 Pokhrel R., et al., 2020, [ApJ](#), 896, 60
 Pokhrel R., et al., 2021, [ApJ](#), 912, L19
 Salim D. M., Federrath C., Kewley L. J., 2015, [ApJ](#), 806, L36
 Schneider S., Elmegreen B. G., 1979, [ApJS](#), 41, 87
 Skrutskie M. F., et al., 2006, [AJ](#), 131, 1163
 Utomo D., et al., 2018, [ApJ](#), 861, L18
 Zuckerman B., Evans N. J., 1974, [ApJ](#), 192, L149

This paper has been typeset from a $\text{\TeX}/\text{\LaTeX}$ file prepared by the author.